Supplementary Information for

Opening of a Cryptic Pocket in β-lactamase Increases Penicillinase Activity

Catherine R Knoverek, Upasana L Mallimadugula, Sukrit Singh, Enrico Rennella, Thomas E Frederick, Tairan Yuwen, Shreya Raavicharla, Lewis E Kay, and Gregory R Bowman

Gregory R. Bowman
Email: g.bowman@wustl.edu

This PDF file includes:

Supplementary Text

Materials and Methods

Mutagenesis and protein purification

We previously cloned the genes for TEM and CTX-M-9 β-lactamase into pET24-b plasmids (Life Technologies) for inducible protein expression under the T7 promoter.(1, 2) Both plasmids use kanamycin resistance for selection and the TEM plasmid contains the OmpA signal sequence for periplasmic export. MTB and GNCA were cloned into pET28 plasmids by Genewiz for inducible protein expression under the T7 promoter. Both plasmids use kanamycin resistance for selection. The MTB plasmid contains an N-terminal 6x His tag with thrombin cleavage site, and the GNCA plasmid contains the OmpA signal sequence for periplasmic export. We created protein variants using site-directed mutagenesis and verified the mutations via DNA sequencing. For expression, we transformed our desired plasmid into BL21(DE3) cells (Intact Genomics) and grew cultures to an OD_{600} of 0.6 before we induced protein expression by adding 1 mM IPTG. TEM, MTB, and GNCA were expressed overnight at 18°C, while CTX-M-9 was expressed for at least three hours at 37°C.

We purified TEM and GNCA using our previously described protocol(1) that isolates the protein from the periplasm using the following osmotic shock lysis protocol. We harvested cells and resuspended them in 30 mM Tris, pH 8.0 with 20% sucrose. After centrifugation, we resuspended the cells in 5 mM $MgSO_4$ at 4°C. After another centrifugation, we dialyzed the supernatant against 20 mM sodium acetate, pH 5.5 overnight at 4°C. We centrifuged the dialysis contents to remove any insoluble protein and then purified using cation exchange chromatography (BioRad UNOsphere Rapid S column) with an NaCl gradient. The final purification step was size exclusion chromatography (BioRad ENrich SEC 70 column), and we stored the purified protein at 4°C in 20 mM Tris, pH 8.0.

We purified CTX-M-9 as previously described(2) by isolating the protein from inclusion bodies using the following protocol. We harvested cells and resuspended them in 20 mM sodium acetate, pH 5.5 and froze them at -80°C at least overnight. We then thawed the cells and lysed them via sonication. We centrifuged the lysate, and resuspended the pellet in 20 mM sodium acetate, pH 5.5 + 9 M urea overnight. After centrifugation, we refolded the protein by adding it drop-wise to buffer with no urea while gently stirring. We removed aggregated protein by centrifugation and dialyzed the supernatant against 20 mM sodium acetate, pH 5.5 overnight at 4°C. After centrifuging the dialysis contents to remove any insoluble protein, we then purified using cation exchange chromatography (BioRad UNOsphere Rapid S column) with an NaCl gradient. The final purification step was size exclusion chromatography (BioRad ENrich SEC 70 column), and we stored the purified protein at 4°C in 20 mM Tris, pH 8.0.

We purified MTB by isolating the protein from the cytoplasm using the 6x His tag and the following protocol. Cells were harvested and resuspended in 25 mM Tris, pH 7.5 + 300 mM NaCl and frozen at -80°C overnight. Cells were then thawed and lysed via sonication. The lysate was centrifuged to remove cell debris and the supernatant was loaded onto a Ni-NTA agarose column. Elution peak fractions were then dialyzed against 25 mM Tris, pH 7.5 + 300 mM NaCl overnight at 4°C. The dialysis contents were centrifuged to remove any insoluble protein before the 6x His tag was removed by thrombin cleavage. The reaction was carried out overnight at room temperature while stirring. The reaction contents were centrifuged to remove any insoluble protein and then cleaved protein was isolated by collecting the flow-through of a Ni-NTA agarose column run. The final purification step was size exclusion chromatography (BioRad ENrich SEC 70 column), and the purified protein was stored at 4°C in 20 mM Tris, pH 8.0.

Labeling assays

For pocket determination, we labeled 5-30 μM protein with 2 mM DTNB (Ellman's reagent, Thermo Scientific) in 20 mM Tris, pH 8.0 at 25°C until completion. We monitored the reaction via a change in absorbance at 412 nm over time using a Cary 100 UV–Vis spectrophotometer (Agilent Technologies). Each measurement was performed in triplicate. We determined the number of cysteines that labeled by first using a series of exponentials fit to the data and then by normalizing the signal using the known protein concentration and Beer's Law (below). Here, l is the pathlength of the cuvette, which is one cm, and ε is the extinction coefficient of TNB at 412 nm, which is 14,150 M^{-1} cm^{-1}.(3)

$$Absorbance = l * \varepsilon * [protein] \quad (1)$$

For labeling of the Ω-loop pocket of the TEM variants, we labeled 10 μM protein with various concentrations of DTNB (Ellman's reagent, Thermo Scientific) in 20 mM Tris, pH 8.0 at 25°C until completion. We introduced an S243C mutation in order to observe pocket opening via labeling, as previous described.(2) We monitored the reaction via a change in absorbance at 412 nm over time using a Cary 100 UV–Vis spectrophotometer (Agilent Technologies) and performed measurements at each DTNB concentration in triplicate. Next, we fit a single exponential equation to the data to obtain the observed rate constants and plotted these values as a function of DTNB concentration. We fit the Linderstrøm-Lang model(4) (below) to the observed rate constants as a function of DTNB concentration to obtain the open pocket population, and obtained error using bootstrapping. We find that the TEM variants reported in this study displayed labeling in the EXX (full expression) or EX2 regime. The EX2 regime is the limiting case when the rate of pocket closing is much faster than the intrinsic rate of labeling, and the observed rate depends linearly on the DTNB concentration.

$$k_{obs} = \frac{k_{op} * k_{int} * [DTNB]}{k_{op} + k_{cl} + k_{int} * [DTNB]} \quad (2)$$

$$k_{obs,EX2} = \frac{k_{op}}{k_{cl}} * k_{int} * [DTNB] = K_{op/cl} * k_{int} * [DTNB] \quad (3)$$

Here, k_{obs} is the observed labeling rate, k_{op} is the rate of pocket opening, k_{cl} is the rate of pocket closing, and k_{int} is the intrinsic labeling rate. We previously measured the intrinsic labeling rate (6.83 sec^{-1} mM^{-1}) by performing the same labeling experiment but on a five amino acid peptide of protein sequence containing the cysteine of interest.(2) The equilibrium constant for pocket opening ($K_{op/cl}$) should be greater than the equilibrium constant for unfolding, which was measured using urea denaturation experiments (see supplemental methods). We used the equilibrium constant for wild type TEM unfolding in equation (3) to calculate k_{obs} as a function of DTNB concentration due to unfolding (dashed line in main text Figure 5a).

Activity assays

We measured the initial velocity (v_i) of antibiotic degradation by β-lactamase at 25°C via a change in absorbance (232 nm for benzylpenicillin, 262 nm for cefotaxime) using a Cary 100 UV–Vis spectrophotometer (Agilent Technologies). The substrate (5-200 μM) was incubated at 25°C for 5 min before addition of the protein. We diluted purified protein to a final concentration no greater than 200 nM. Our activity buffer was 50 mM potassium phosphate, pH 7.0 with 10% glycerol, and we measured each substrate concentration in triplicate. For benzylpenicillin, the Michaelis-Menton equation (below) was fit to the initial velocity as a function of the substrate concentration to determine individual catalytic rate (k_{cat}) and Michaelis constant (K_M) values. Here, $[E]$ is the total enzyme concentration, and $[S]$ is the total substrate concentration. For

cefotaxime, the K_M was too high to reach maximum velocity, so a line (below) with a slope equal to $[E] * \frac{k_{cat}}{K_M}$ was fit to the data. Error for the fit parameters was determined using bootstrapping.

$$v_i = \frac{[E] * k_{cat} * [S]}{K_M + [S]} \tag{4}$$

$$v_i = [E] * \frac{k_{cat}}{K_M} * [S] \tag{5}$$

NMR CEST experiments

We recorded all experiments on a Bruker AVANCE III HD 18.8 T spectrometer equipped with a cryogenically cooled, x,y,z pulsed-field gradient triple-resonance probe. We recorded each D-CEST(5, 6) experiment (30°C) as a pseudo-3D matrix, where each 2D spectrum were obtained as a function of the position of weak B_1 perturbations applied at discrete frequencies overt the chemical shift range of the probed nucleus. We applied a DANTE excitation scheme,(7) which perturbs multiple regularly spaced frequencies at the same time, thereby decreasing the frequency range that must be explored over regular CEST approaches. In all cases, we calibrated the strength of the B_1 field using a nutation experiment, as described previously.(8)

We acquired ^{15}N D-CEST data as previously described(5) using 1 s DANTE excitation trains of square pulses (~7° flip angle, 2.5 kHz B_1 field) and an interpulse delay of 2, 1, and 0.667 ms, resulting in effective B_1 fields of about 10, 20, and 30 Hz. We sampled CEST profiles in 51 steps, with increments of 10, 20, and 30 Hz, extending over frequency ranges of 500 (2 ms interpulse delay), 1000 (1ms), and 1500 Hz (0.667 ms), respectively. We extracted the position of the minor dips, exchange rate, and population of the excited state by fitting a two-state model of chemical exchange to the CEST data as described in detail previously.[32] Errors were estimated using the bootstrapping.

Molecular dynamics simulations and analysis

We prepared systems as previously described,(9) using GROMACS software(10) and the Amber03 force field.(11) We solvated in TIP3P water(12) and energy minimized using the steepest descent algorithm. We used the V-rescale thermostat to maintain a fixed temperature of 300K and the Berendsen barostat to bring the pressure up to one bar. Mutations were introduced into the starting structure using PyMol.

We ran 200 nanoseconds of metadynamics simulations on each variant using the PLUMED plugin on GROMACS(13) and defined our collective variable (s) using the backbone torsional angles of the 238-loop. This collective variable is expressed using the equation below.

$$s = \frac{1}{2}\sum_{i}^{n}\left[1 + \cos\left(\phi_i - \phi_i^{Ref}\right)\right] \tag{6}$$

Here, ϕ_i is the torsion angle of dihedral i of the current frame in the simulation and ϕ_i^{Ref} is a reference torsion angle defined by the corresponding dihedral in the crystal structure. This summation is done across n dihedrals. We computed our collective variable using the ϕ and ψ angles of residues that underwent CEST, namely residues 237 through 243. Gaussians were added every 2 picoseconds with a height of 1.0 kJ/mol and a width of 0.05.
We clustered our metadynamics simulations using a hybrid k-centers/k-medoids algorithm(14) to generate 220 representative seed conformations, using a cluster radius cutoff of 1.2 Å. We then used these conformations to collect a total of 100.7 microseconds of unbiased simulations on our Folding@home distributed computing platform.(15)

To analyze our simulation data, we first built a Markov state model (MSM) using our Enspara software (simulation data is available at: https://osf.io/gyxtu/).(16) We again clustered using a hybrid k-centers/k-medoids algorithm and used a cluster radius cutoff of 1.2 Å, which resulted in 9877 states. A pseudo-count was added to each element in the transition counts matrix to prevent sampling artifacts from influencing the transition probabilities.

We then used the CARDS methodology(17) to compute the holistic communication ($I_H(X,Y)$) for every pair of dihedrals X and Y using the equation below.

$$I_H(X,Y) = \overline{I_{ss}(X,Y)} + \overline{I_{sd}(X,Y)} + \overline{I_{ds}(X,Y)} + \overline{I_{dd}(X,Y)} \quad (7)$$

Here, $\overline{I_{ss}(X,Y)}$ is the normalized mutual information between the structure (i.e., rotameric state) of dihedral X and the structure of dihedral Y, $\overline{I_{sd}(X,Y)}$ is the normalized mutual information between the structure of dihedral X and the dynamical state of dihedral Y, $\overline{I_{ds}(X,Y)}$ is the normalized mutual information between the dynamical state of dihedral X and the structure of dihedral Y, and $\overline{I_{dd}(X,Y)}$ is the normalized mutual information between the dynamical state of dihedral X and the dynamical state of dihedral Y. The mutual information (I) is described by the equation below.

$$I(X,Y) = \sum_{x \in X} \sum_{y \in Y} p(x,y) \log \left(\frac{p(x,y)}{p(x)p(y)} \right) \quad (8)$$

Here, $x \in X$ refers to the set of possible states that dihedral X can adopt, $p(x)$ is the probability that dihedral X adopts state x, and $p(x,y)$ is the joint probability that dihedral X adopts state x and dihedral Y adopts state y. We computed normalized mutual information using the maximum possible mutual information, known as the channel capacity, for any specific mode of communication. We then computed a community network using affinity propagation,(18) with a damping parameter of 0.8. We generated the final allosteric network by filtering the community network using the Marginal Likelihood Filter (MLF)(19) to capture the top 5% of edges.

Finally, we applied principal component analysis (PCA) to the distances between the Cβ atoms of every pair of residues in the community containing the Ω-loop and catalytic S70. We projected our MSM onto principal components 1 and 3 (PC1 and PC3) and pulled out exemplar structures by estimating the population-weighted centroid of the two minima.

NMR CPMG experiments

We recorded ^{15}N CPMG experiments as previously described,(20) using a **c**onstant-time relaxation interval, T_{relax}, of 30 milliseconds.(21) We sampled 20 ν_{CPMG} values of ≤1 kHz, using CPMG refocusing pulses applied at a $\gamma B_1/2\pi$ = 6 kHz field and phase-modulated according to the {x,x,y,-y} cycling scheme.(22) We applied a $\gamma B_1/2\pi$ = 15.6 kHz field ^{1}H continuous wave decoupling during T_{relax}. To ensure constant heating in the reference experiments (recorded with T_{relax} equal to 0 seconds), we applied the same ^{1}H continuous wave decoupling immediately prior to the recycle delay.

Urea denaturation experiments

We prepared samples of 35 µg/mL protein in 50 mM potassium phosphate, pH 7.0 at various concentrations of urea and equilibrated the samples at room temperature overnight. After one-minute incubation in an Applied Photophysics Chirascan equipped with a Quantum Northwest Inc. TC125 Peltier-controlled cuvette holder, we monitored circular dichroism (CD) signal at 222 nm. We recorded the signal for one minute at 25°C in a one cm path length quartz cuvette. Then, we measured the refractive indexes of each sample in order to the determine their precise urea concentration. We determined the free energy values by fitting a two-state folding model (below)

to the CD data and using the linear extrapolation method.(23) Each variant was measured in triplicate experiments.

$$CD = \frac{\theta_U + \theta_F * e^{-(\Delta G + m*[urea])/R*T}}{1 + e^{-(\Delta G + m*[urea])/R*T}} \quad (9)$$

Here, θ_U and θ_F are the CD signals for the unfolded and folded states, fit as lines. ΔG is the extrapolated free energy difference between the unfolded and folded states in the absence of urea, and m is the proportionality constant related to the steepness of the folding transition. R is the gas constant and T is temperature.

Urea unfolding kinetics

We prepared a protein sample in 50 mM potassium phosphate, pH 7.0 and samples of various urea concentrations above the concentration midpoint (C_M) in the same buffer. After five-minute incubation in an Applied Photophysics Chirascan equipped with a Quantum Northwest Inc. TC125 Peltier-controlled cuvette holder, we added the protein to the urea buffer, diluting the protein to a final concentration of 35 μg/mL, and manually mixed by inverting the cuvette. We then monitored the circular dichroism (CD) signal at 222 nm over time at 25°C in a one cm path length quartz cuvette. We measured the refractive indexes of each sample in order to the determine their precise urea concentration. An exponential was fit to each unfolding kinetic trace to determine the observed unfolding rate at that given urea concentration. The unfolding rate in the absence of urea was then calculated using a linear extrapolation fit to the log of the observed unfolding rates as a function of urea.

Fig. S1. Shown is the structure of the TEM β-lactamase acyl-intermediate bound to benzylpenicillin (PDB: 1fqg). Serine-70 and glutamic acid-166, important catalytic residues, are shown in sticks.

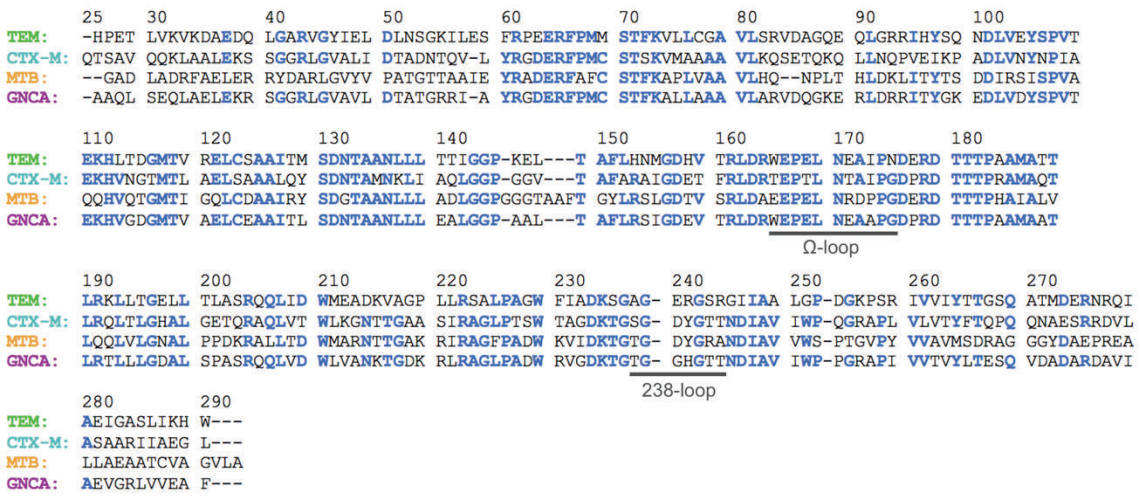

Fig. S2. β-lactamase homologs have the same topology, but only share about 50% sequence identity. The sequence alignment for the four homologs discussed in this study is shown here, with conserved residues shown in blue. The Ω-loop and 238-loop sequences are underlined.

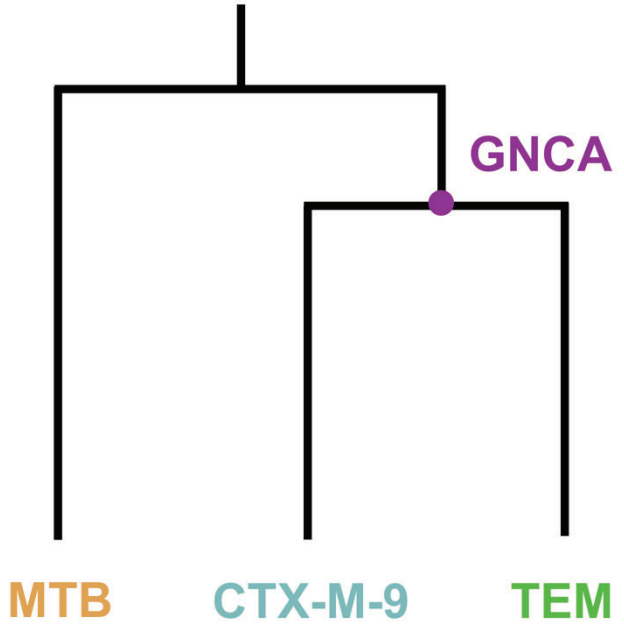

Fig. S3. TEM, CTX-M-9, and MTB are modern-day homologs, while GNCA is the predicted ancestral sequence of TEM and CTX-M-9. Shown is a not-to-scale representation of the evolutionary relationship between the four homologs discussed in this study.

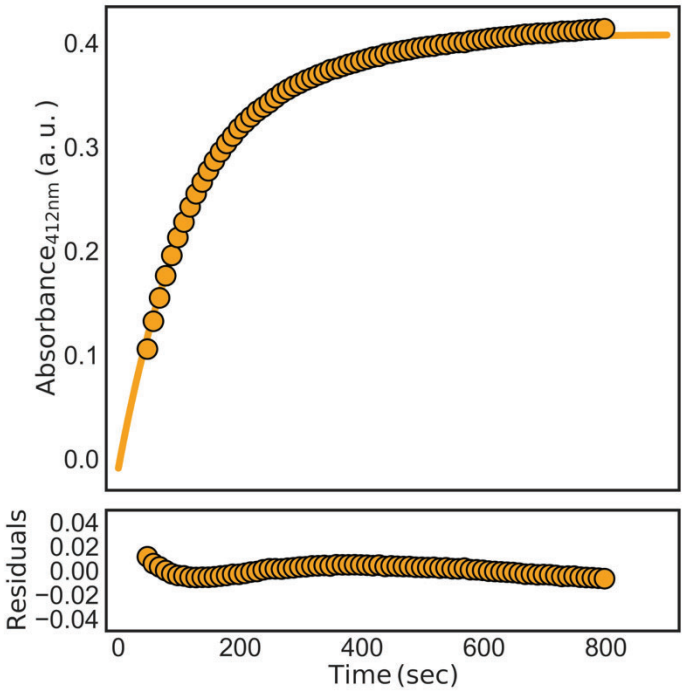

Fig. S4. Labeling of WT MTB is well-fit by a single exponential. Shown here is the average labeling trace for 30 μM protein and 2 mM DTNB. Raw data is shown as circles and the fit is shown as a solid line. Below are the residuals for the fit.

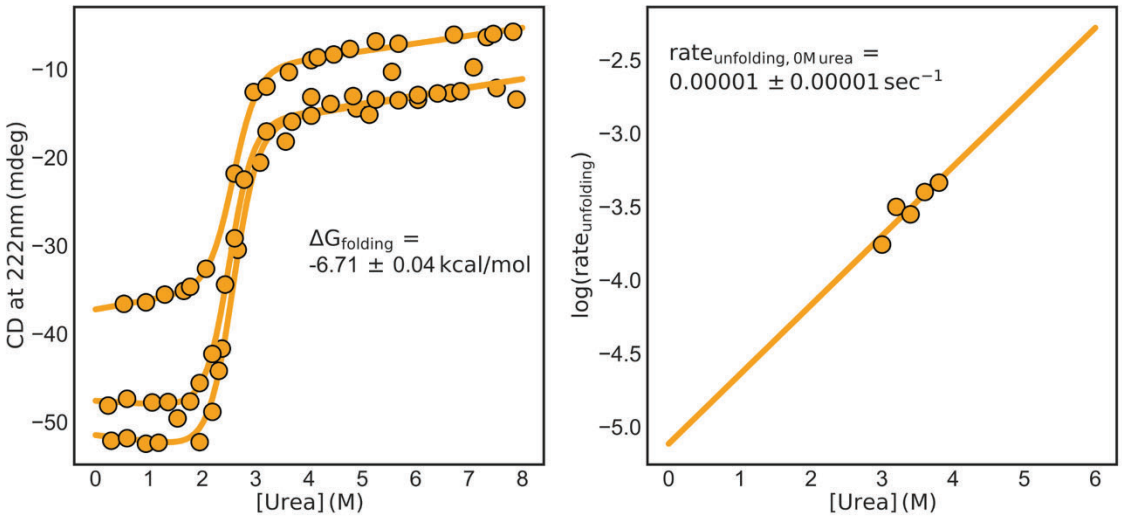

Fig. S5. Labeling of WT MTB was not due to protein unfolding. (Left) Urea denaturation was followed by circular dichroism. Error is reported as the standard deviation of three replicate experiments. (Right) The unfolding rate was monitored by circular dichroism and then plotted as a function of urea concentration. The y-intercept of the fit line represents the unfolding rate in the absence of urea.

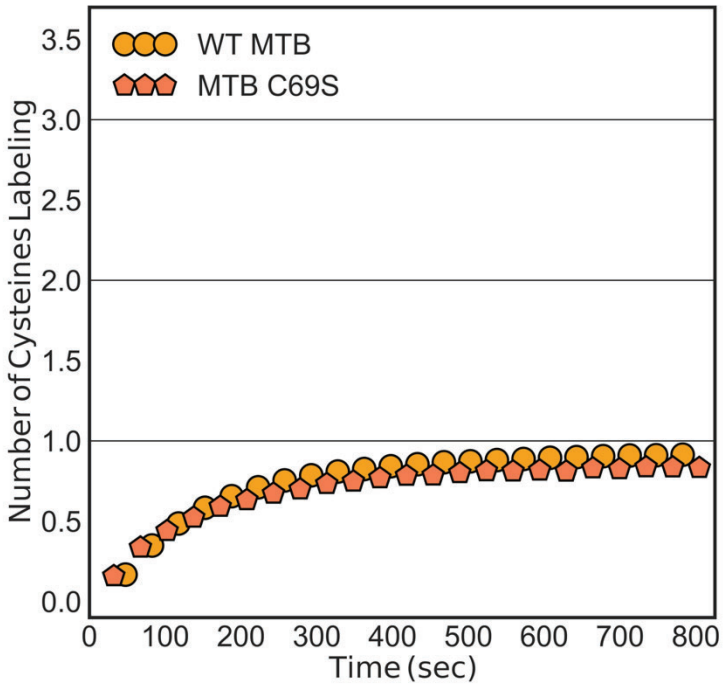

Fig. S6. Mutating out the cysteine residue in the Ω-loop pocket region, C69, does not reduce labeling. The normalized DTNB labeling of MTB C69S (coral pentagons) overlays well with the labeling of WT MTB (orange circles), both which plateau at one cysteine labeling.

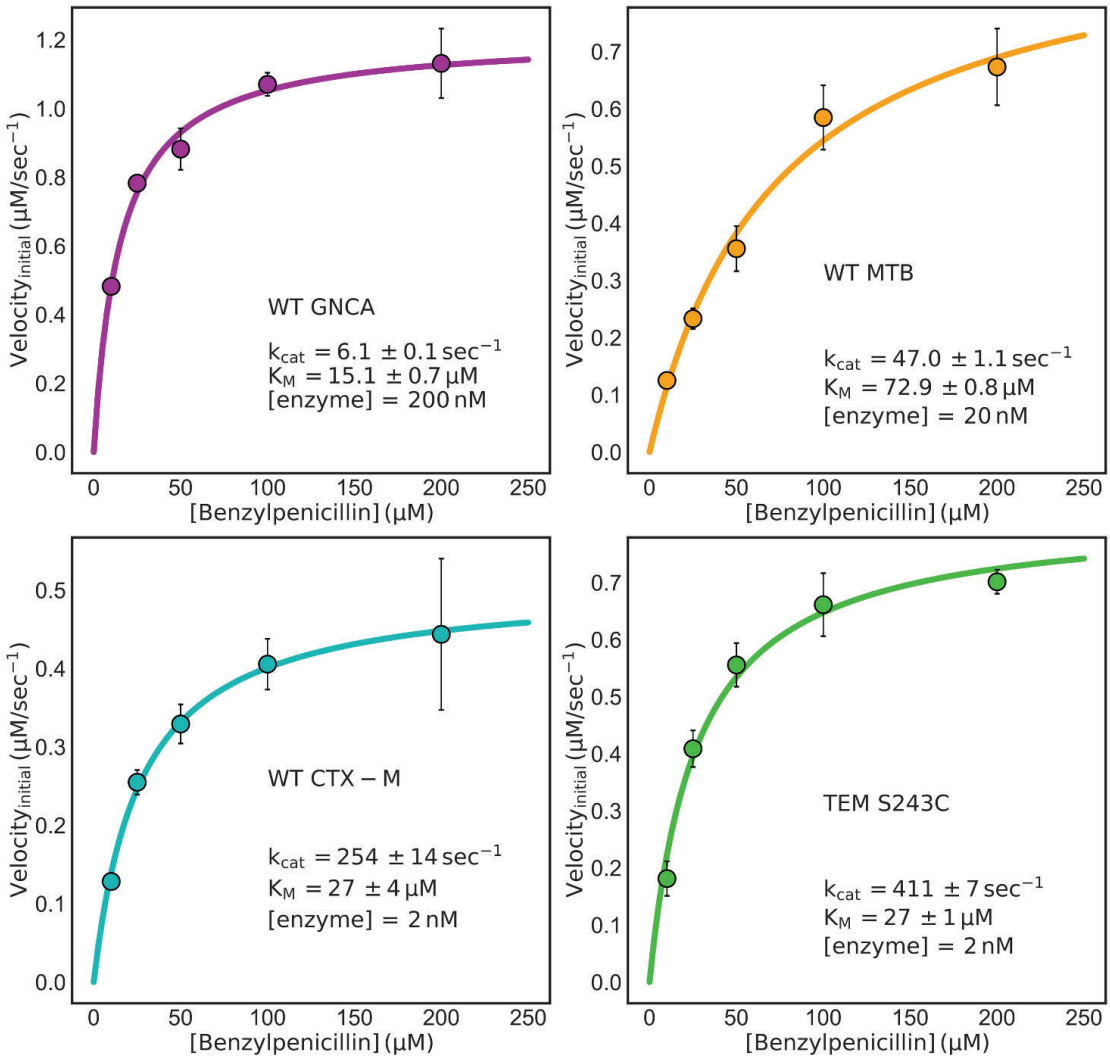

Fig. S7. β-lactamases with Ω-loop pockets have higher catalytic rates against benzylpenicillin. The full Michaelis-Menten equation was fit to the data. Error bars are shown as the standard deviation of three replicate measurements. Error for each parameter was determined using bootstrapping.

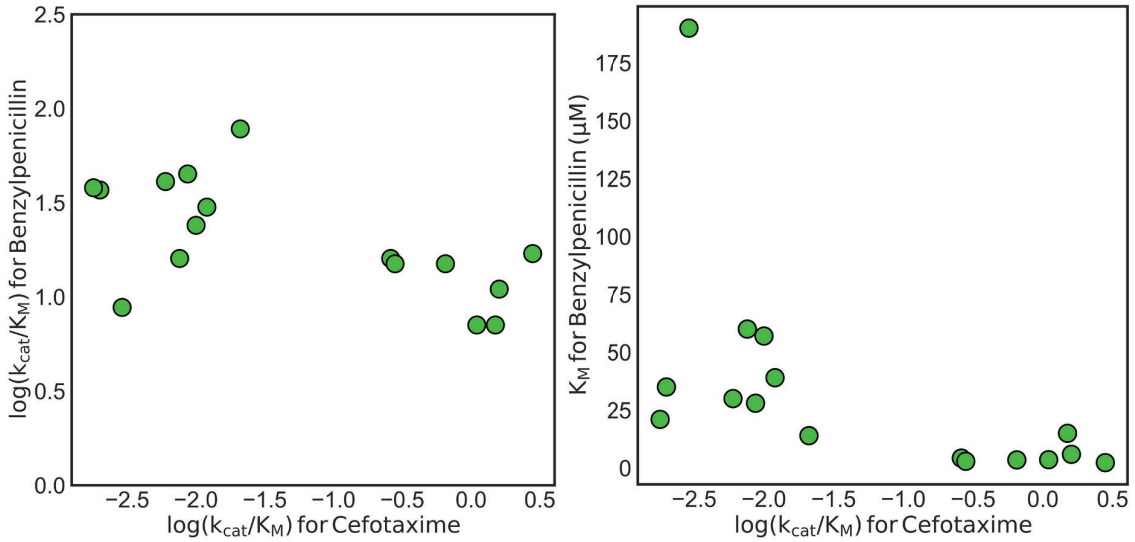

Fig. S8. The correlation between the catalytic efficiencies for benzylpenicillin and cefotaxime is weaker and appears to be due to a compensating decrease in benzylpenicillin K_M as k_{cat} decreases. (Left) Shown is the correlation between the catalytic efficiency for benzylpenicillin and the catalytic efficiency for cefotaxime. (Right) Shown is the correlation between the Michaelis constant for benzylpenicillin and the catalytic efficiency for cefotaxime. Each point represents a different TEM variant. The outlying variants from main text Figure 3, R164E/G238S and R164D/G238S, are not included here.

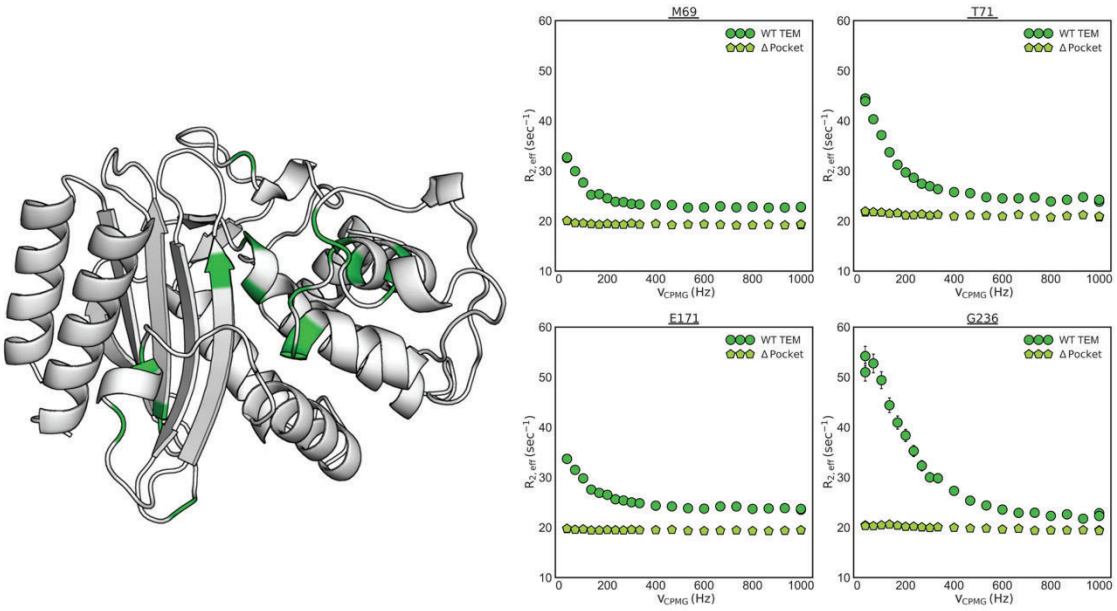

Fig. S9. The R241P mutation in TEM removes dynamics on the microsecond to millisecond timescale as monitored by relaxation dispersion. (Left) Highlighted in green on the wild type (WT) TEM structure (PDB: 1xpb) are the residues showing conformational exchange as established by Car-Purcell-Meiboom-Gill (CPMG) experiments. (Right) ^{15}N CPMG profiles for wild type TEM (green circles) and TEM R241P, a variant with no Ω-loop pocket, (light green pentagons) are shown for a set of representative residues.

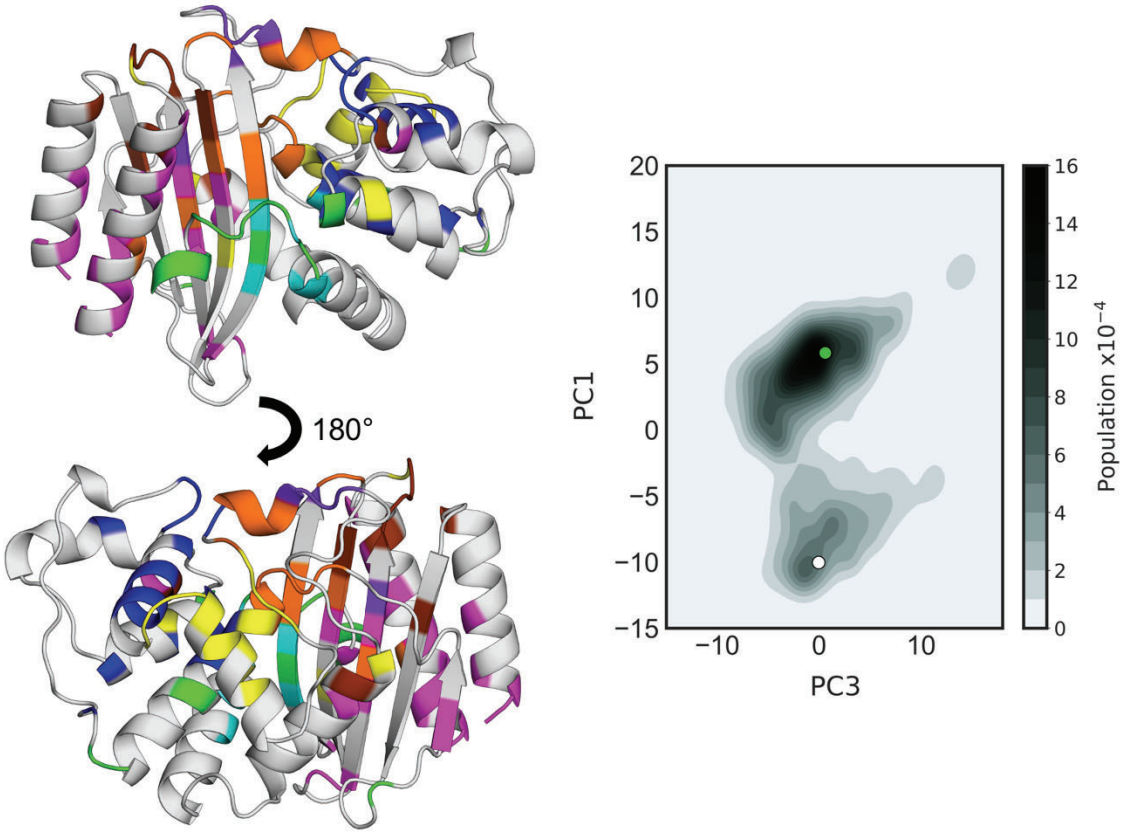

Fig. S10. Simulation data was analyzed using CARDS and PCA. (Left) Each color highlighted on the WT TEM structure (pdb: 1xpb) represents a different CARDS community. These communities are residues which have correlated dihedral motions. The orange community includes the Ω-loop and the catalytic S70. (Right) We performed PCA on the orange community and found two resolved minima. The colored circles represent the positions of the exemplar structures shown in main text figure 4b.

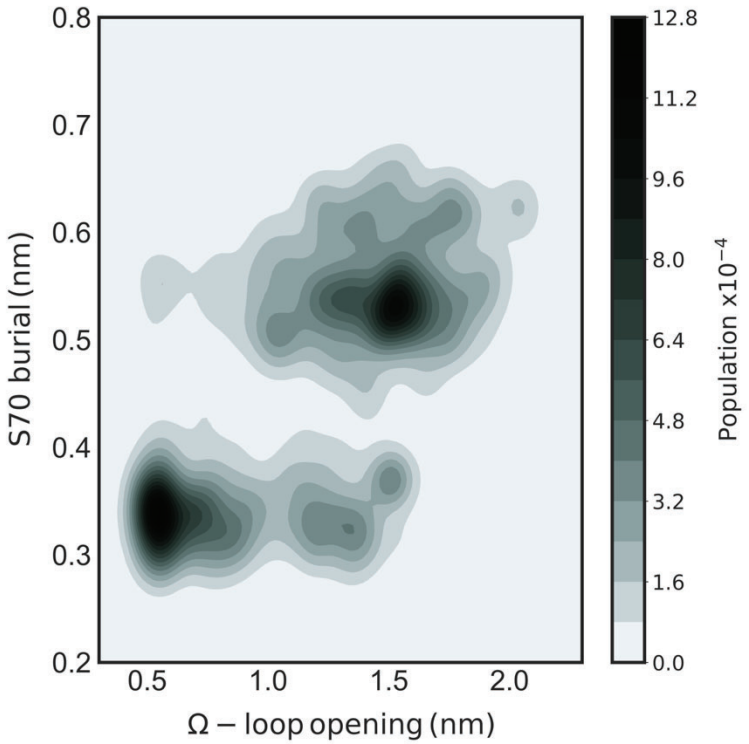

Fig. S11. Ω-loop pocket opening is correlated with S70 burial. A 2D histogram of catalytic S70 burial as a function of Ω-loop pocket opening shows that when the pocket is open, S70 is predominantly buried. S70 burial is captured using a backbone hydrogen bond distance between S70 and K73. The Ω-loop opening distance is characterized by the Cα-Cα distance between E240 and E171.

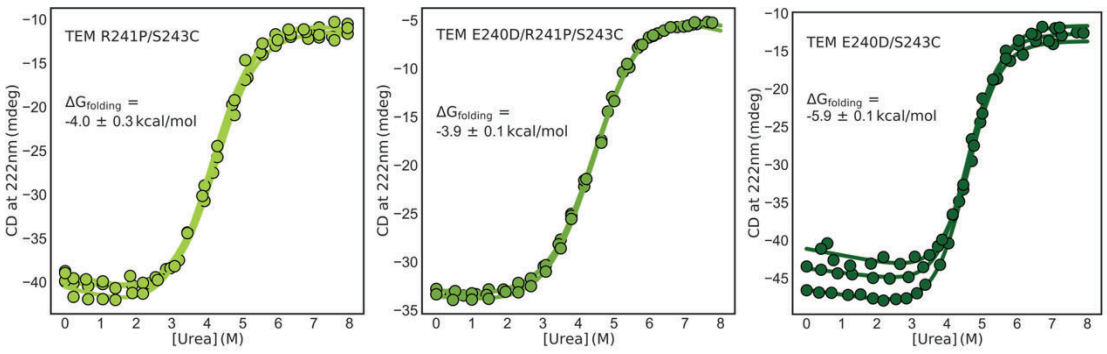

Fig. S12. The labeling rates for TEM R241P are on the order of magnitude as those expected for labeling due to protein unfolding, while the rates for TEM E240D are much faster. Urea denaturation was followed by circular dichroism for TEM R241P (left), TEM E240D/R241P (middle), and TEM E240D (right). Error is reported as the standard deviation of three replicate experiments. The S243C mutation is needed for thiol labeling measurements and is included for all variants.

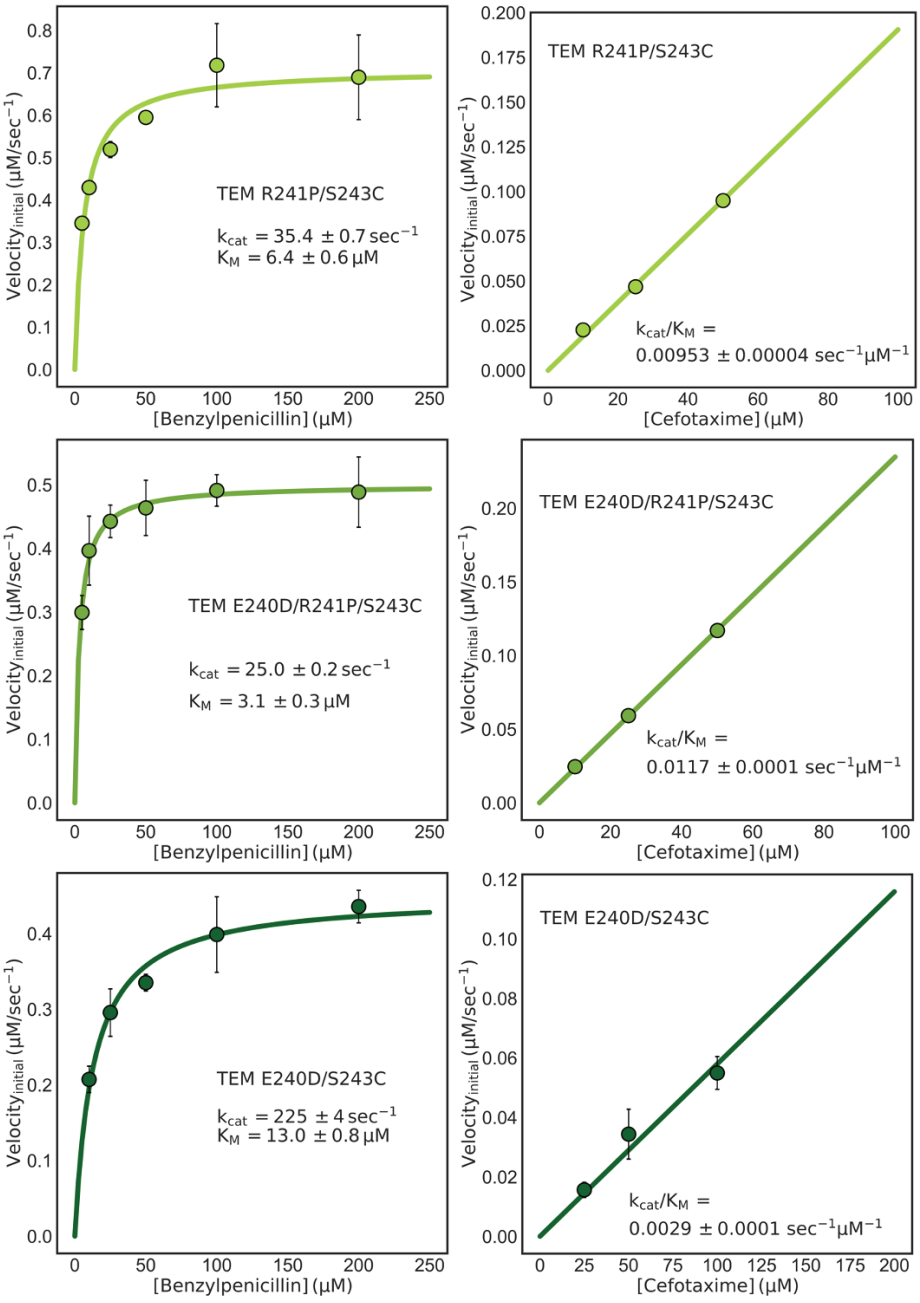

Fig. S13. The R241P mutation increases cefotaxime activity and decreases benzylpenicillin activity, while the E240D mutation decreases cefotaxime activity and increases benzylpenicillin activity. The full Michaelis-Menten equation was fit to the benzylpenicillin activities. A line with a slope equal to the catalytic efficiency multiplied by the enzyme concentration was fit to the cefotaxime activities. Error bars are shown as the standard deviation of three replicate measurements. Error for each parameter was determined using bootstrapping. The S243C mutation is needed for thiol labeling measurements and is included for all variants.

Table S1. In order to determine existence of the Ω-loop pocket, the pocket population should be higher than the unfolded population.

TEM Variant	Ω-Loop Pocket Open Population (%)	Unfolded Population (%)
Wild Type (S243C)†	1.1 ± 0.2‡	0.02 ± 0.01†
E240D/S423C	4 ± 1◇	0.0047 ± 0.0009
R241P/S243C	0.002 ± 0.005*	0.12 ± 0.07
E240D/R241P/S243C	0.19 ± 0.01	0.14 ± 0.02

† The S243C mutation is needed for thiol labeling measurements and is included for all variants
‡ Porter *et al.*, 2019
◇ Labeling in the EXX regime, individual k_{op} and k_{cl} were determined and then divided to obtain the $K_{op/cl}$
*Determined to not have an Ω-loop pocket as the pocket population is less than the unfolded population

SI References

1. K. M. Hart, C. M. Ho, S. Dutta, M. L. Gross, G. R. Bowman, Modelling proteins' hidden conformations to predict antibiotic resistance. *Nat Commun* **7**, 12965 (2016).

2. J. R. Porter *et al.*, Cooperative Changes in Solvent Exposure Identify Cryptic Pockets, Switches, and Allosteric Coupling. *Biophys J* **116**, 818-830 (2019).

3. H. B. Collier, Letter: A note on the molar absorptivity of reduced Ellman's reagent, 3-carboxylato-4-nitrothiophenolate. *Anal Biochem* **56**, 310-311 (1973).

4. A. Berger, K. Linderstrom-Lang, Deuterium exchange of poly-DL-alanine in aqueous solution. *Arch Biochem Biophys* **69**, 106-118 (1957).

5. T. Yuwen, L. E. Kay, G. Bouvignies, Dramatic Decrease in CEST Measurement Times Using Multi-Site Excitation. *Chemphyschem* **19**, 1707-1710 (2018).

6. T. Yuwen, G. Bouvignies, L. E. Kay, Exploring methods to expedite the recording of CEST datasets using selective pulse excitation. *J Magn Reson* **292**, 1-7 (2018).

7. G. A. Morris, R. Freeman, Selective excitation in Fourier transform nuclear magnetic resonance. 1978. *J Magn Reson* **213**, 214-243 (2011).

8. M. Guenneugues, P. Berthault, H. Desvaux, A method for determining B1 field inhomogeneity. Are the biases assumed in heteronuclear relaxation experiments usually underestimated? *J Magn Reson* **136**, 118-126 (1999).

9. G. R. Bowman, P. L. Geissler, Equilibrium fluctuations of a single folded protein reveal a multitude of potential cryptic allosteric sites. *Proc Natl Acad Sci U S A* **109**, 11681-11686 (2012).

10. M. J. Abrahama; Teemu, M.; Schulzbc, R.; Pálla, S.; Smith, J.C.; Hessa, B.; Lindahlad, E., GROMACS: High performance molecular simulations through multi-level parallelism from laptops to supercomputers. *SoftwareX* **1-2**, 19-25 (2015).

11. Y. Duan *et al.*, A point-charge force field for molecular mechanics simulations of proteins based on condensed-phase quantum mechanical calculations. *J Comput Chem* **24**, 1999-2012 (2003).

12. W. L. Jorgensen, J. Chandrasekhar, J. D. Madura, R. W. Impey, M. L. Klein, Comparison of Simple Potential Functions for Simulating Liquid Water. *Journal of Chemical Physics* **79**, 926-935 (1983).

13. G. A. Tribello, M. Bonomi, D. Branduardi, C. Camilloni, G. Bussi, PLUMED 2: New feathers for an old bird. *Comput Phys Commun* **185**, 604-613 (2014).

14. K. A. Beauchamp *et al.*, MSMBuilder2: Modeling Conformational Dynamics at the Picosecond to Millisecond Scale. *J Chem Theory Comput* **7**, 3412-3419 (2011).

15. M. Shirts, V. S. Pande, COMPUTING: Screen Savers of the World Unite! *Science* **290**, 1903-1904 (2000).

16. J. R. Porter, M. I. Zimmerman, G. R. Bowman, Enspara: Modeling molecular ensembles with scalable data structures and parallel computing. *J Chem Phys* **150**, 044108 (2019).

17. S. Singh, G. R. Bowman, Quantifying Allosteric Communication via Both Concerted Structural Changes and Conformational Disorder with CARDS. *J Chem Theory Comput* **13**, 1509-1517 (2017).

18. B. J. Frey, D. Dueck, Clustering by passing messages between data points. *Science* **315**, 972-976 (2007).

19. N. Dianati, Unwinding the hairball graph: Pruning algorithms for weighted complex networks. *Phys Rev E* **93**, 012304 (2016).

20. D. F. Hansen, P. Vallurupalli, L. E. Kay, An improved 15N relaxation dispersion experiment for the measurement of millisecond time-scale dynamics in proteins. *J Phys Chem B* **112**, 5898-5904 (2008).

21. F. A. Mulder, N. R. Skrynnikov, B. Hon, F. W. Dahlquist, L. E. Kay, Measurement of slow (micros-ms) time scale dynamics in protein side chains by (15)N relaxation dispersion NMR spectroscopy: application to Asn and Gln residues in a cavity mutant of T4 lysozyme. *J Am Chem Soc* **123**, 967-975 (2001).

22. B. Jiang, B. Yu, X. Zhang, M. Liu, D. Yang, A (15)N CPMG relaxation dispersion experiment more resistant to resonance offset and pulse imperfection. *J Magn Reson* **257**, 1-7 (2015).

23. T. O. Street, N. Courtemanche, D. Barrick, Protein folding and stability using denaturants. *Methods Cell Biol* **84**, 295-325 (2008).